Acoustic Sensing of Ocean Mixed Layer Depth and Temperature from Uplooking ADCPs

SAMUEL BRENNER,[a] JIM THOMSON,[a] LUC RAINVILLE,[a] DANIEL TORRES,[b] MARTIN DOBLE,[c] JEREMY WILKINSON,[d] AND CRAIG LEE[a]

[a] *Applied Physics Laboratory, University of Washington, Seattle, Washington*
[b] *Woods Hole Oceanographic Institution, Woods Hole, Massachusetts*
[c] *Polar Scientific Ltd., Appin, United Kingdom*
[d] *British Antarctic Survey, Cambridge, United Kingdom*

(Manuscript received 31 May 2022, in final form 15 September 2022)

ABSTRACT: Properties of the surface mixed layer (ML) are critical for understanding and predicting atmosphere–sea ice–ocean interactions in the changing Arctic Ocean. Mooring measurements are typically unable to resolve the ML in the Arctic due to the need for instruments to remain below the surface to avoid contact with sea ice and icebergs. Here, we use measurements from a series of three moorings installed for one year in the Beaufort Sea to demonstrate that upward-looking acoustic Doppler current profilers (ADCPs) installed on subsurface floats can be used to estimate ML properties. A method is developed for combining measured peaks in acoustic backscatter and inertial shear from the ADCPs to estimate the ML depth. Additionally, we use an inverse sound speed model to infer the summer ML temperature based on offsets in ADCP altimeter distance during open-water periods. The ADCP estimates of ML depth and ML temperature compare favorably with measurements made from mooring temperature sensors, satellite SST, and from an autonomous Seaglider. These methods could be applied to other extant mooring records to recover additional information about ML property changes and variability.

KEYWORDS: Ocean; Arctic; Acoustic measurements/effects; In situ oceanic observations; Instrumentation/sensors

1. Introduction

Arctic Ocean interactions with either the sea ice or the atmosphere are modulated by the ocean mixed layer (ML), where surface heat and momentum exchanges are linked to deeper waters (e.g., Toole et al. 2010). ML properties such as depth and temperature are critical variables for understanding and predicting the changing Arctic. Making sustained measurements of these variables in the region near the sea surface is challenging, primarily because of the presence of sea ice.

A variety of platforms provide measurements of ML properties, though these are both spatially and temporally scattered (Peralta-Ferriz and Woodgate 2015). Traditional shipboard sampling of water column properties is seasonally biased toward open-water periods, and regions where navigation is easier; i.e., thinner-ice regions. Ice-tethered profilers (ITPs; Krishfield et al. 2008; Toole et al. 2010) provide a growing resource of year-round upper-ocean measurements under sea ice in the Arctic, helping alleviate some issues with shipboard sampling. ITPs are deployed on drifting multiyear ice floes and not fixed in space, so they allow for an understanding of the seasonal evolution of the ML in the sea ice reference frame. Characterizing ML development over the sea ice–to–open-water transition or looking at interannual variability would benefit from additional Eulerian sampling. Moorings are useful platforms for providing long-term records of oceanographic conditions at fixed locations in the Arctic (e.g., Lin et al. 2019; Polyakov et al. 2020a; Fine and Cole 2022); however, measurements of the ML in the Arctic Ocean from moorings can be particularly challenging. Due to the presence of sea ice, moorings deployed in the Arctic have no surface expression and the uppermost subsurface floats on these moorings must be sufficiently deep to avoid sea ice keels (e.g., Krishfield et al. 2014), and are thus unable to measure the shallow MLs characteristic of the spring and summer season (e.g., Peralta-Ferriz and Woodgate 2015; Gallaher et al. 2016; Cole et al. 2017).

This study demonstrates that upward-looking acoustic Doppler current profilers (ADCPs) installed on subsurface floats are capable of estimating both the depth and temperature of the Arctic Ocean ML. As ADCPs are commonly included on moorings, this methodology may allow for additional data recovery and value from preexisting mooring arrays.

Observations from the Beaufort Sea, including moorings measurements, autonomous assets, and remote sensing, and are described in section 2. Signatures of the ML manifest in the ADCP measurements from each of the moorings as peaks in acoustic backscatter and inertial velocity shear; section 3 presents an approach for finding these peaks and merging them into an annual time series of ML depth, and compares the results with observations of the vertical temperature structure at the moorings. ADCP measurements of ice draft (from

Denotes content that is immediately available upon publication as open access.

Brenner's current affiliation: Brown University, Providence, Rhode Island.

Corresponding author: Samuel Brenner, sdbrenner@brown.edu

DOI: 10.1175/JTECH-D-22-0055.1

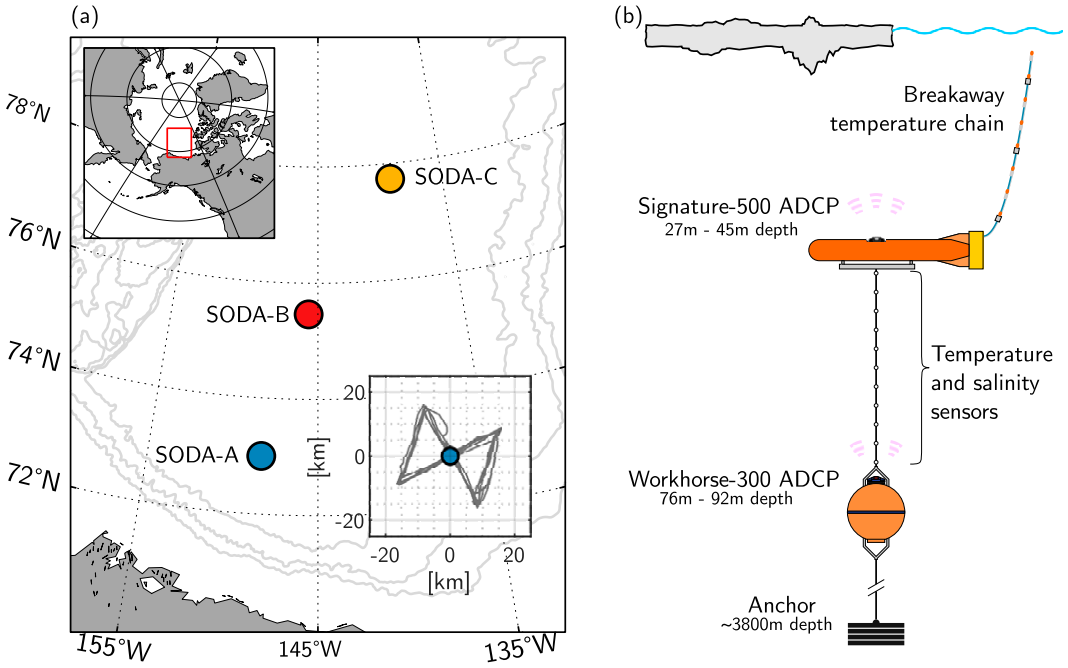

FIG. 1. (a) Maps showing the locations of the moorings, with insets showing (top left) the map location and (bottom right) the Seaglider track in the vicinity of SODA-A. Gray contours show 1000 m isobaths. (b) Schematic of mooring instrument configuration.

a vertical altimeter beam) can be used to infer the surface ML temperature during summer. In open water, nonzero measurements of sea ice draft reflect variations in acoustic travel time due to differences in the speed of sound in the warmer surface layer. Using the results from section 3 together with these erroneous ice draft measurements, section 4 describes the construction of a two-layer inverse sound speed model that can be used to predict the ML temperature.

2. Measurements

The Office of Naval Research (ONR) Stratified Ocean Dynamics of the Arctic (SODA) research program (Lee et al. 2016) included the installation of three subsurface moorings in the deep Canada Basin of the Beaufort Sea (~3800 m water depth) from fall 2018 to 2019 (Fig. 1; and see Brenner et al. 2021). The moorings are designated, from south to north, as SODA-A, SODA-B, and SODA-C (Fig. 1a). They were highly instrumented in the top ~90 m of the water column (Fig. 1b) to measure upper-ocean temperature, salinity, and velocity, along with sea ice drift speed and geometry. Estimates of ML depth and ML temperature were made using ADCP measurements from these moorings and compared to upper-ocean temperatures collected both by the moorings and by an autonomous instrument and remote sensing.

a. *ADCP measurements*

Each of the three moorings included two upward-looking ADCPs installed on floats at different depths. The top float of each mooring, a DeepWater Buoyancy StableMoor (see Harding et al. 2017), housed a Nortek Signature-500 (hereafter SIG500) 5-beam ADCP. A syntactic foam float ~45–50 m deeper contained a Teledyne Workhorse-300 (hereafter WH300) ADCP (Fig. 1b). The depths of each of the top floats were ~45 m for SODA-A, 42 m for SODA-B, and 27 m for SODA-C (a float depth of 45 m was targeted for all three moorings, but logistical constraints during deployment resulted in a shallower depth at SODA-C). The distance between the upper and lower instruments was fixed except for small adjustments due to line creep through the year, and when currents inclined the moorings. During strong currents, the top float at SODA-B had a maximum vertical deviation of ~14 m from its resting position; vertical deviations were even smaller at the other moorings. Data from the SIG500 ADCPs were previously presented by Brenner et al. (2021), and the concurrent sampling schemes used with those instruments are described in that paper. Velocity measurements from both ADCPs were merged together to create a continuous product within the top ~80 m of the water column, with a 2 m vertical bin spacing and a temporal resolution of 1 h.

To focus on vertical shear only at the base of the ML, we consider the shear corresponding specifically with inertial oscillations, which are associated with "slab-like" motion of the ML (e.g., Pollard and Millard 1970). Horizontal velocities (u, v) were filtered to retain the clockwise-rotating near-inertial frequency band using complex demodulation (Tukey 1961) with a fourth-order low-pass Butterworth filter applied with a frequency with a cutoff of 0.1f. The inertial frequencies (periods) at each of the three moorings were: 1.395×10^{-4} rad s^{-1} (12.51 h), 1.412×10^{-4} rad s^{-1} (12.36 h), and 1.412×10^{-4} rad s^{-1} (12.25 h), for SODA-A to SODA-C, respectively, so the filter

TABLE 1. Acoustic parameters used for determining the relative backscatter, SV for each instrument and mooring, based on the fitting procedure described by Gostiaux and van Haren (2010).

	SIG500			WH300		
	A	k_c	E_{noise}	A	k_c	E_{noise}
SODA-A						
Beam 1	48.99	0.88	18.48	54.16	0.55	41.00
Beam 2	48.80	0.87	18.07	53.64	0.55	40.00
Beam 3	48.21	0.85	18.50	56.11	0.55	44.00
Beam 4	46.98	0.85	18.38	57.66	0.55	45.00
SODA-B						
Beam 1	47.68	0.89	17.85	43.60	0.38	39.00
Beam 2	47.85	0.89	17.68	41.88	0.35	42.00
Beam 3	49.41	0.94	17.95	45.86	0.35	45.00
Beam 4	48.85	0.93	17.88	43.82	0.35	46.00
SODA-C						
Beam 1	42.17	0.80	18.00	57.29	0.55	44.00
Beam 2	40.33	0.74	17.83	49.76	0.42	43.00
Beam 3	43.00	0.76	19.88	49.38	0.44	41.00
Beam 4	44.25	0.80	19.87	54.63	0.52	41.00

bandwidth was ~2.5 h. The inertial shear magnitude is $S_I = [(\partial u_I/\partial z)^2 + (\partial v_I/\partial z)^2]^{1/2}$, where subscript I refers to the inertially filtered velocities.

The echo intensity/amplitude recorded from each of the ADCPs were treated separately (i.e., the Signature500 and WH300 echo data on each mooring were not merged). For each record, the relative acoustic backscatter (SV) was found from the recorded echo data by accounting for acoustic transmission loss and beam spreading following Gostiaux and van Haren (2010), which is based on Deines (1999) but with empirical fits of the scale factor k_c and a more careful accounting for signal-to-noise ratios near the noise floor. The relative backscatter is calculated as

$$\text{SV} = I_{\text{dB}} - A + 20\log R + 2\alpha R, \tag{1}$$

where R is a distance from the instrument, A is an empirical constant value that incorporates transmit power and geometric factors, α is a frequency-dependent attenuation coefficient [taken as 0.069 for the WH300s (Deines 1999) and 0.146 for the SIG500s, calculated from Francois and Garrison (1982)], and I_{dB} is a relative acoustic intensity (in dB) derived from the recorded echo intensity, E after scaling and subtracting noise:

$$I_{\text{dB}} = 10\log(10^{k_c E/10} - 10^{k_c E_{\text{noise}}/10}). \tag{2}$$

The fitted values of A, k_c, and E_{noise} for each of the instruments are shown in Table 1. Note that while the values of SV will vary somewhat if calculated for different accepted values of these parameters [e.g., using the constant value of $k_c = 0.45$ from Deines (1999) for WH300 instruments], the overall results of this study—which are based just on identifiable peaks in SV profiles—are relatively insensitive [e.g., in a similar procedure, Macrander et al. (2007) simply use the echo amplitude E after removing an exponential fit]. Acoustic reflections of other mooring components were frequently seen in the echo data from the deeper WH300 ADCPs, so contaminated bins were removed, as identified based on the magnitude of the annually averaged error velocity (using a threshold of 1.5×10^{-3} m s^{-1}). In addition to reflections from the pycnocline that are used to determine ML depth (section 3), the acoustic backscatter also recorded signals of biological activity in the water column including both the diel vertical migration of zooplankton (e.g., Dmitrenko et al. 2020, 2021), and seasonal differences that might be associated with the phytoplankton bloom (e.g., Ardyna et al. 2014). The signal associated with diel vertical migration produced peaks in backscatter that competed with the pycnocline reflection, so to minimize this impact we averaged the acoustic backscatter in daily time bins. This smears out the signal of the diel migration while leaving the peak associated with the ML depth relatively intact.

Altimeter distances from the vertical beam of the SIG500 were corrected for ADCP tilt, speed of sound (measured at the instrument), and atmospheric pressure variations (Brenner et al. 2021). Sea ice draft was calculated as the difference between the instrument depth H (based on pressure measurements; instrument accuracy 10% of pressure range) and the altimeter distance D. Altimeter burst measurements were categorized as being either sea ice or open water based on their spectral properties following Shcherbina et al. (2016; also see Kirillov et al. 2020; Brenner et al. 2021). In sea ice cover, the difference between the instrument depth H (based on pressure measurements) and the altimeter distance D was used to calculate sea ice draft: $d = H - D$. For bursts identified as being in open water (based on spectral characteristics), erroneous nonzero values of d (i.e., nonzero values of ice draft) indicate water column sound speed variations due to shallow stratification (section 4).

b. *Temperature and salinity measurements*

On each of the moorings, the ~45 m distance between the two ADCPs was instrumented with a set of Seabird SBE37 MicroCAT conductivity–temperature–depth (CTD) sensors and SBE56 temperature (T) sensors (Fig. 1b). A total of 10 of sensors (6 SBE37 and 4 SBE56) were installed with a spacing of ~4–5 m between instruments, and instrument types alternating. At all three of the moorings, the uppermost SBE37 (positioned directly underneath the topmost float) failed sometime during the summer season (between late May and early July), but pressure and temperature measurements made by the SIG500 ADCP itself continued to provide a record at that float throughout the full data record, albeit with a decreased temporal resolution and accuracy (prior to failure, the uppermost SBE37 was used to correct and calibrate the SIG500 temperature measurements).

In addition, a 40-m-long, buoyant "breakaway chain" of high-spatial-resolution (0.25 m spacing) temperature sensors was attached to the tail of the StableMoor (the topmost float) in order to measure temperatures shallower than the float depth. These sensors measured with a 3-h sampling period.

The chain was built up of 8 sections that were each 5 m long (a total length of 40 m) and connected with a set of weak links of progressively increasing strength. All data collected by the sensors along the chain were recorded by a datalogger housed in the StableMoor float. This allowed for sections of the chain to break off without the loss of data as they were raked by passing sea ice keels. The breakaway chains were successfully deployed for SODA-A and SODA-C. At SODA-B, a rough sea state during (anchor-last) mooring deployment resulted in the chain fouling with the main mooring line and no data above the StableMoor. At SODA-C, which was located in perennial sea ice cover, the shallower top float depth (~27 m) resulted in some chain sections being initially against the ice at the surface, so most of the chain broke away shortly after deployment. Of the eight chain sections, five of them (the top 25 m) had broken off by 12 October 2018 (less than 1 week after deployment). An additional 5 m section broke off on 11 March 2019, leaving only two sections (10 m) for the remainder of the deployment. At SODA-A, one section broke away on 18 December 2018, and a second section was lost 19 February 2019; the other six sections (30 m) of the chain remained intact. Pressure sensors located at distances of 5, 20, and 35 m along each of the chains allowed for reconstruction of their positions in the water column and the depths of each of the temperature sensors. This was done using a quadratic model fit to the available pod distances and pressures (which decreased in number as chain sections broke away) including the pressure measured by the Signature500 ADCPs at distance 0. The pressure measurements show that the strong ocean currents at SODA-A (up to 0.5 m s^{-1}) resulted in significant movement and frequent "blow down" of the chain (in extreme cases, the vertical extent measured by the chain was <5 m even when the chain was 30 m long). At SODA-C, which was more quiescent, the chain was usually fairly vertical. There were occasional data spikes or dropouts along some sections of the breakaway chain. These were more prominent at SODA-A (possibly due to chain movement which may have disrupted internal cabling), with sections 1 and 3 missing data for most of the year. Though less frequent at SODA-C, similar spikes and dropouts still occurred. Data spikes were most apparent as unphysically high temperatures. To account for these issues, all temperatures above 6.5°C were removed from the record of both moorings, and temperatures were interpolated across data gaps and dropouts. Measurements were then bin averaged in 2-m along-chain (8 sensor) bins. Some noise and horizontal banding remaining in the final data record shows some calibration offsets/errors associated with individual sensors that could not be resolved.

Temperatures and salinity measurements made by the Seabird sensors on the mooring line and by the breakaway chains were both temporally averaged into 1-day bins (note that inspection of temperature sections from the breakaway chains prior to averaging did not reveal significant subdaily variations in the apparent ML depth). Measured temperatures and salinities were converted to Conservative Temperature and Absolute Salinity using the Gibbs Seawater Oceanographic toolbox (IOC et al. 2010); references to temperature and salinity made in section 4 refer to those quantities.

In addition to the mooring measurements, an autonomous Seaglider (SG229) sampled temperature and salinity from 16 August to 30 September 2019 in a 20 km "bow-tie" pattern around SODA-A, with a mean distance from the mooring of ~12 km (Fig. 1a). The Seaglider is a small, reusable, long-range autonomous underwater vehicle designed to glide from the ocean surface to 1000 m and back while collecting profiles of temperature, salinity, and other oceanic variables. Gliders steer through the water by controlling attitude (pitch and roll) and can thus navigate between waypoints to execute survey patterns, in this case with successive dives separated by ~4 km, and ~6.5 h. Temperature and salinity were measured by SG229 were averaged into 1 m vertical bins and temporally averaged into 1-day bins for consistency with the other data sources. It is not possible to completely separate the effects of temporal and spatial variability measured by the Seaglider. Nonetheless, ML properties measured by the Seaglider did not vary considerably across the bow-tie pattern. Over any individual bow-tie track, ML-averaged temperature anomalies (relative to a linear trendline over the whole record) had a maximum standard deviation of 0.29°C, and there was no correlation of those anomalies with position. Below the ML, there are some minor differences in the "patchiness" of the temperature profiles between the Seaglider and the mooring data (not shown), which suggest some spatial variability in subsurface eddy features over the sampling area. This subsurface spatial variability is unlikely to impact any of the conclusions of the present study.

In situ measurements were supplemented with satellite-derived sea ice concentrations (A) and sea surface temperatures (SSTs) provided by the Operational Sea Surface Temperature and Sea Ice Analysis (OSTIA) data product (Donlon et al. 2012). These are provided at daily intervals at 0.05° resolution. Data were interpolated to provide time series of A and SST at SODA-A.

3. ML depth

a. *Approach*

Sharp temperature and salinity gradients cause reflections of acoustic signals due to changes in acoustic impedance (e.g., Ross and Lavery 2012), so peaks in measured acoustic reflectance (backscatter) can be related to stratification (e.g., Shibley et al. 2020). Furthermore, particles (e.g., plankton) can accumulate at the ML boundary (e.g., Möller et al. 2012), which can further enhance backscatter there. These principles have been used to identify oceanic structures from acoustic echo sounder or seismic data (e.g., Penrose and Beer 1981; Holbrook and Fer 2005; Stranne et al. 2017; and others; including of the Arctic ML; Stranne et al. 2018).

Peaks in stratification are also often a location of strong vertical shear of horizontal velocity. The ocean ML responds directly to wind forcing (e.g., Price et al. 1987; Randelhoff et al. 2014; Chaudhuri et al. 2021). Particularly for inertial oscillations, which are rotational motions of the ML at the local Coriolis frequency, the velocity profile is generally more or less uniform in the ML (the "slab" models of Pollard and

TABLE 2. ML depth algorithm parameters for each of the data sources. Threshold identifies the minimum peak prominence used for identifying local maxima. Depth range identifies the vertical bounds of the search algorithm for each of the two seasons. Date range shows when data from each instrument were considered. R.S. = record start; R.E. = record end; F.R. = full record.

	WH300 backscatter	SIG500 backscatter	Inertial shear
Threshold	0.5 dB	1.5 dB	1.5×10^{-3} s^{-1}
Depth range			
Winter	25–70 m	—	6–70 m
Summer	—	6–40 m	6–40 m
Date range			
SODA-A	14 Nov 2019–12 Jun 2019	12 Jun 2019–R.E.	F.R.
SODA-B	R.S.–15 Jun 2019	4 Jul 2019–R.E.	F.R.
SODA-C	R.S.–15 Jun 2019	18 Jul 2019–R.E.	F.R.

Millard 1970; D'Asaro 1985), with strong inertial shear at the ML base. Because of the slab-like structure of inertial oscillations, inertial shear will be relatively weak within the ML and have a strong signal at the ML base. As such, inertial-band shear is likely a better indicator of the ML depth than broadband shear (which would likely include other signals within the ML; e.g., due to mixing layer development).

Macrander et al. (2007) previously showed that a seafloor mounted ADCP could be used to identify the interface depth of a deep exchange flow: the Denmark Strait Overflow. Those authors considered both echo intensity (a measure of acoustic backscatter) and shear separately to construct and compare different time series of Denmark Strait Overflow interfacial depth. As both shear and backscatter in the surface ML can be impacted by a variety of processes absent in deeper overflow water, we adapt and build on the ideas presented by Macrander et al. (2007) in order to develop a methodology for identify the ML depth from moored (uplooking) subsurface ADCPs.

Here, the ML depth is identified using ADCP measurements of inertial shear and acoustic backscatter together. An overview of the procedure is as follows:

1) For each of the data sources (WH300 backscatter, SIG500 backscatter, inertial shear), identify ML depth at each time step from local maxima, subject to constraints on "peak prominence" and the depth range considered (see below).
2) Combine individual ML depth measurements for separate sources into a single time series for each season.
3) Perform a weighted-moving average.

Steps are described below in more detail. These steps were performed separately for "winter" and "summer" seasons to account for different ML characteristics: deeper MLs throughout the ice-covered period of the year, with a shift to shallow MLs with the injection of freshwater from melting sea ice (Peralta-Ferriz and Woodgate 2015). Different constraints on the depth range considered were used for each season. The delineation between these seasons was chosen manually based on visual inspection of backscatter and shear, in which we looked for the time at which both shear and backscatter showed a developing and coherent near-surface signal. Winter/summer boundaries were identified as 12 June, 4 July, and 18 July 2019 for SODA-A, SODA-B, and SODA-C, respectively; before these dates was considered "winter," and afterward was considered "summer." The method for ML depth identification would be improved by a more objective identification of the onset of the shallow summer stratification, but we were unable to identify a satisfactory approach for this that was robust to measurement noise/variability. At all three moorings these dates correspond to sea ice concentrations of $A \sim 68\%$. It is likely that summer freshwater layers were present earlier than these dates, but were too shallow to be identified (the shallowest resolvable ADCP measurements were ~6 m deep due to surface sidelobe reflection).

Step 1. Rather than identifying the ML as the absolute maximum values of shear or backscatter for a given time step (as in Macrander et al. 2007), we searched for local maxima. At each time step, we associated the ML with the shallowest local maxima whose peak extends above background values by some minimum threshold, and is within a specified depth range (with different depth bounds for the search algorithm for winter and summer seasons, and for different data sources; Table 2). This was done separately for each of the three data sources, using the MATLAB *findpeaks* function with a "minimum peak prominence." Peak thresholds were chosen ad hoc after inspecting the data fields (Table 2). ML depths were only identified for times when there were peaks that met the threshold value. For each of the identified peaks, a three-point quadratic stencil was applied to points centered on the peak, with the ML depth taken as depth of the maximum of the quadratic fit (Figs. 2d,e). The three-point stencil allows for the determination of ML depth values between ADCP measurement bins. The inertial shear magnitude often showed multiple additional peaks below the ML (Fig. 2a). For this reason, variability in the strength of inertial shear peaks relative to the assigned threshold can lead to "jumps" in the identified ML depth (e.g., in late February Fig. 2a); this is why both shear and backscatter signals are used together (step 2) and subsequently smoothed (step 3) to create the final ML product.

Step 2. For each season, individual ML depth points from the different sources (backscatter and shear) were combined into a single time series. Due to instrument limitations (depth and range) and environmental differences, the blended data

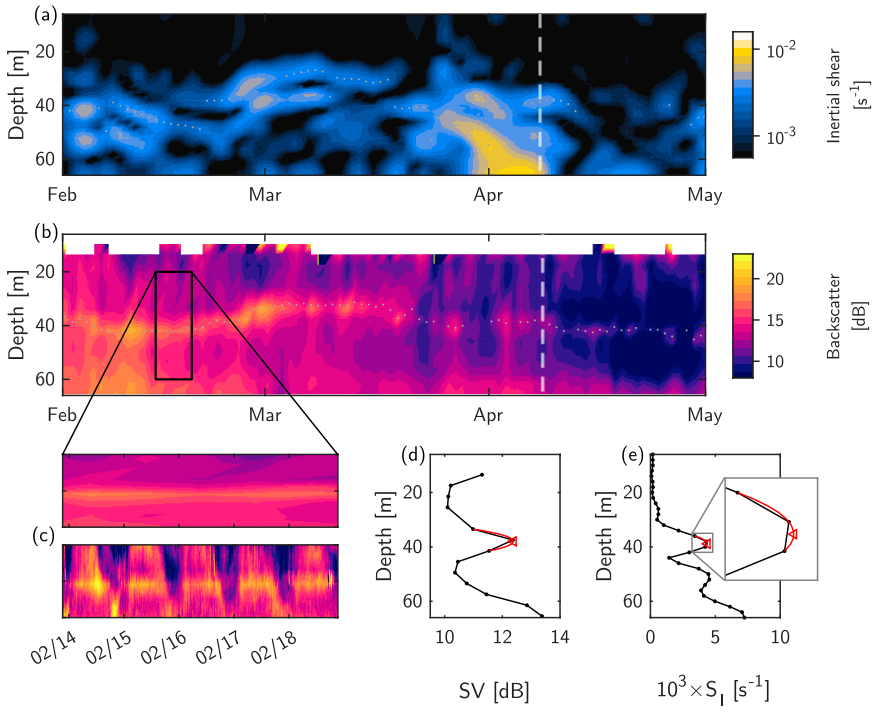

FIG. 2. Example of ML depth identification from a 3-month period in winter/spring 2019 at SODA-C, showing time series of (a) inertial shear magnitude (S_I) and (b) daily averaged relative acoustic backscatter (SV). Points in (a) and (b) show identified ML depths. (c) An inset from (b) demonstrating the effects of diel migration on backscatter and showing (top panel) the daily averaged backscatter used for identifying the ML and (bottom) the same data before averaging. (d),(e) The peak identification for individual profiles of (d) backscatter and (e) shear, including the subgrid three-point stencil [inset in (e)] for the times identified by vertical dashed lines in (a) and (b).

included different data from different data sources during different times of the year. In particular, elevated midwater column backscatter during sea ice breakup and open water (possibly due to seasonal phytoplankton bloom) partly obfuscated WH300 backscatter measurements, and lead to the divergence of peaks found in backscatter and inertial shear. As inertial shear is more representative of ML dynamics, we took this divergence as an indication that those backscatter data were not reflective of ML depth. For this reason, backscatter-derived ML depth points from the WH300 were included during winter only. While these effects were also present in the SIG500 backscatter, they were minimized by the shallower depths of those instruments. Depths from the SIG500 backscatter were included during summer only, when MLs would be consistently above those instruments. Inertial shear data were included throughout the full year, as summarized in Table 2.

Step 3. A smoothed daily ML depth time series was constructed by taking the weighted averages of depths in centered moving 7-day windows. Weights were calculated as the prominence of each peak (from the peak detection algorithm) normalized by the minimum threshold for each data type; this gives higher weights to peaks associated with strong acoustic reflection or shear. The distribution of weights associated with the different data sources were generally similar: weight values for shear and SIG500 backscatter were mostly between 1 and 5, with means of ~2–2.5, while for WH300 the range was slightly higher with means ~4–5. For windows containing 3 or fewer measurements, no calculation was performed. Finally, days in which no averages were reported due to lack of data were filled in with linear interpolation. At SODA-B and SODA-C, linear interpolation accounted for a minimal amount of the record, filling in 10 and 6 days total, respectively, and with the longest gap at either mooring being 4 days. At SODA-A, ML detection was more challenging (ocean conditions there were more variable) and required longer periods of interpolation. This record contained a number of gaps up to 1 week long (e.g., during the passage of a large eddy in early November) and a total of 46 days of interpolated ML depths.

Figure 2 provides an example of the ML depth identification procedure from a 3-month period in winter at SODA-C (including a view of the diel variations of acoustic backscatter). The figure demonstrates the variability in the signals of both backscatter and shear.

b. *Results*

Figure 3 shows time series of the ML depths found for each mooring. At all moorings, the method produced ML depths

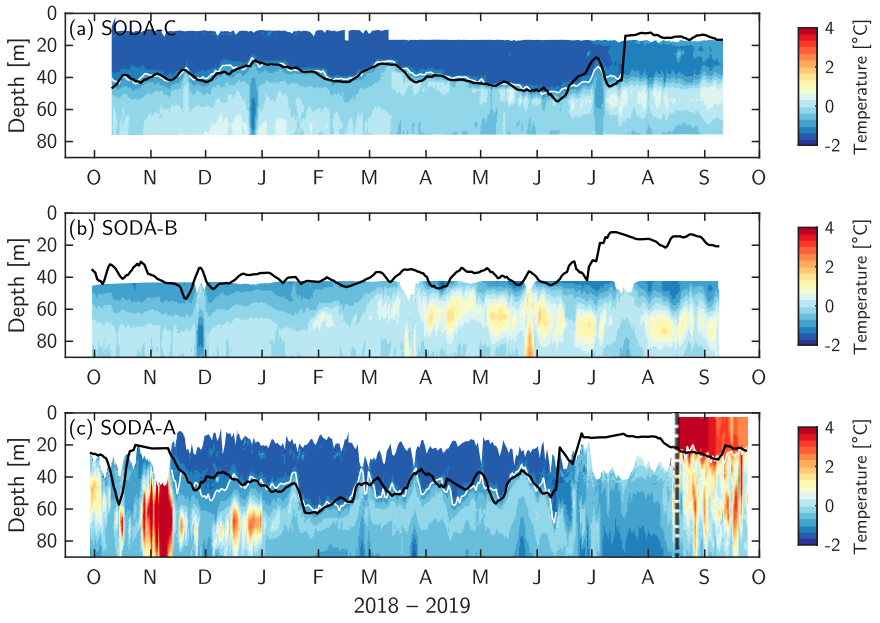

FIG. 3. Time series of upper-ocean temperatures at each of the three moorings (as labeled from north to south). (c) SODA-A, with temperatures from mooring measurements prior to 16 Aug 2019 and from the Seaglider after that date [(c) delineated by a vertical dash–dotted line]. (b) SODA-B and (a) SODA-C, with temperature measurements are only from the mooring. Black lines in each panel show the final ML depth time series identified through shear and backscatter (i.e., independent of temperature measurements). White contours in (a) and (c) show the ML depth based on the −1°C isotherm (through winter) or from the peak N from Seaglider measurements [(c); summer].

similar to recent measurements in the same region (Cole et al. 2017), with winter mean ML depths of 42.7, 40.0, and 39.7 m, for SODA-A to SODA-C, respectively, and mean summer depths of 20.2, 16.2, and 14.4 m. Cole et al. (2017) found ML depths of 40 m in winter and depths 10–15 m at the beginning of summer, which deepened through September.

The ML depths determined from ADCP shear and backscatter (black line in Fig. 3) followed variations in the measured upper-ocean temperature from the moorings and Seaglider. Wintertime variability in ADCP-derived ML depth corresponded to vertical displacement of isotherms, and tracked the depth of a strong vertical temperature gradient. To quantify the fit, the −1° isotherm was taken as representative of the winter ML depth from SODA-A and SODA-C mooring sections (since the surface water was at the freezing temperature during winter ice cover, this corresponds to a ΔT threshold of ~0.5°–0.6°). The −1° isotherm was chosen as it generally tracks local peaks of dT/dz (which are likely collocated with peaks in buoyancy frequency), but calculation/identification was less impacted by measurement noise in the breakaway chain (which is amplified when taking gradients). From August–September at SODA-A, a ML depth was defined based on the depth of the maximum buoyancy frequency, N, from the Seaglider measurements. These ML depths are shown as white contours in Fig. 3.

There is good correspondence between the ADCP-estimated ML and that determined from the mooring/Seaglider sections (Fig. 4). Correlation coefficients and root-mean-square errors were $r = 0.60$, RMSE = 8.28 m for SODA-A, and $r = 0.88$, RMSE = 2.67 m for SODA-C. The approach used to identify ML depths from the ADCP measurements is entirely independent of the temperature–salinity data, so the ML depths determined using those measurements corroborate this method.

At SODA-B, where shallower temperature data were less available, direct comparisons or validation of the estimated ML depths was not possible. Nonetheless, some of the temporal variations in the ML depth during winter at that mooring match with the heaving of isotherms deeper in the water column (Fig. 3b).

Aside from when the Seaglider measurements were available, temperature data were too deep in the water column to compare ML depth measurements during the summer shallow ML period. This highlights the limitations of using those data to investigate summer MLs, and the value of being able to derive those measurements from ADCPs.

4. ML temperature

a. Approach

The advent of vertical altimeter beams on some ADCP models allows for measurements of sea ice draft or surface gravity waves (e.g., Magnell et al. 2010; Thomson and Rogers 2014; Kirillov et al. 2020; Brenner et al. 2021; Cooper et al. 2022;

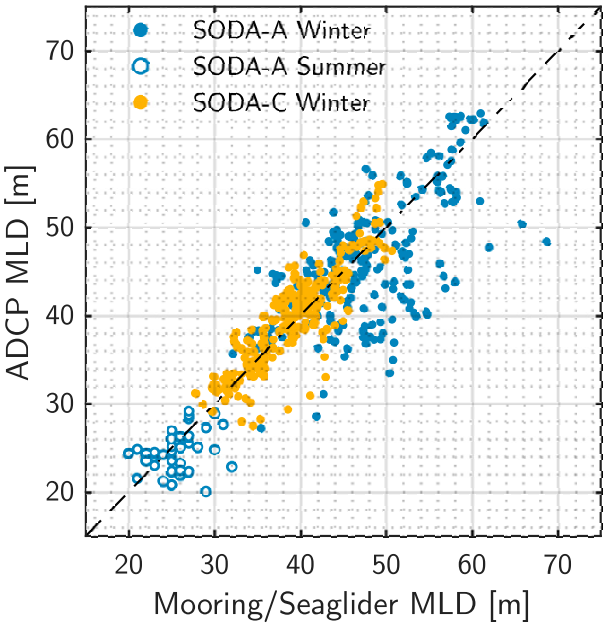

FIG. 4. ML depths based on the −1°C isotherm (SODA-A and SODA-C; winter) or from the peak N in Seaglider measurements (SODA-A; summer) vs ML depths estimated from ADCP-measured shear and backscatter. The black dashed line shows the 1:1 slope.

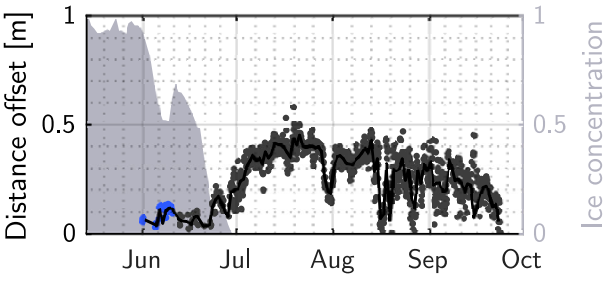

FIG. 5. Distance offset ($H - D$) measurements for burst data at SODA-A identified as open water (left axis), and sea ice concentration (right axis). Points show individual measurements, while the solid line show daily averages. Note that open-water bursts occur for nonzero ice concentration due to measurements between sea ice floes. Blue points at the beginning of the record show times when the ML depth was below the depth of the instrument.

Thomson 2022). However, the presence of surface stratification, such as shallow MLs, leads to small offsets in these altimeter measurements, primarily due to changes in acoustic travel time as a result of vertically varying sound-speed profiles. As such, offsets between the pressure-derived instrument depth H and the altimeter-derived instrument depth D measured in open water have been used to make empirical sound speed corrections to these measurements (e.g., Kirillov et al. 2020; Brenner et al. 2021). Here, we instead make use of those erroneous measurements from a SIG500 ADCP to infer the summertime ML temperature using an inverse sound speed model. As this method requires sufficient sound speed differences between the ML and deeper water and some amount of identifiable open water, it is applicable to summer conditions only. This limitation is not prohibitive as wintertime ML temperatures can already be assumed to be near the local freezing temperature, so it is in the summer conditions when we would be most interested.

We focus only on summer measurements from SODA-A as a demonstrative example. At SODA-A, measurements of $H - D$ in open water reached as high as ~0.5 m (Fig. 5). Shallow stratification can cause errors in these measurements due to both sound speed changes (which impact the altimeter distance, D) and density changes (which impact the conversion from pressure to instrument depth, H). Thus, open-water depth offsets $d = H - D$ can be expressed as $d = \varepsilon_H + \varepsilon_D$, where ε_H and ε_D are the separate errors associated with H and D. While in general these effects cannot be separated, Arctic waters exist in a temperature–salinity regime in which density, and hence ε_H, is set almost entirely by salinity. So ε_H can be estimated separately given an appropriate model of salinity. For the small salinity differences (and thus small salinity-derived ML density variation) predicted here, ε_H is small and most of the error can be attributed to ε_D.

The speed of sound in water is a strong function of temperature. Inverse sound speed models provide a measure of integrated ocean heat content based on observed travel times of acoustic signals (Watts and Rossby 1977). Together with a model for the water column structure, these measurements have been leveraged to determine details of the vertical temperature distribution. For example, Sanchez et al. (2021) use acoustic travel times measured by pressure-sensor-equipped inverted echo sounders (PIES; Meinen and Watts 1998) to investigate temperature and thickness of Atlantic Water inflow to a glacial fjord. Knowing upper- and lower-layer temperatures, Macrander et al. (2007) also makes use of travel time measurements from PIES to estimate the depth interface of the Denmark Strait Overflow (for comparison to the backscatter and shear methods; section 3).

Prior to the onset of the shallow summer stratification, the ML was at the local freezing temperature (Fig. 3). As sea ice concentration decreases and shallow summer stratification sets in, the ML is expected to rapidly warm (e.g., Peralta-Ferriz and Woodgate 2015) while the ocean below the ML remains approximately the same temperature. As a first-order approximation, we model the upper ocean as a two-layer system with a homogeneous surface ML of depth h_1 overlying a lower layer of depth h_2 which has linear temperature and salinity gradients (Fig. 6). The lower-layer gradients dT/dz and dS/dz are assumed to be constant in time. We find these gradients by making linear fits to the average of measurements from the mooring line between July and August 2019 (using only measurements deeper than the SIG500 ADCP); those gradients are extrapolated upward to the base of the ML (at depth h_1). In this way, the profiles of T_2 and S_2 are given as $T_2(z) = T(H) + (dT/dz)(H - z)$, where $T(H)$ is the temperature at the ADCP, taken from the mooring measurements, and equivalently $S_2(z) = S(H) + (dS/dz)(H - z)$.

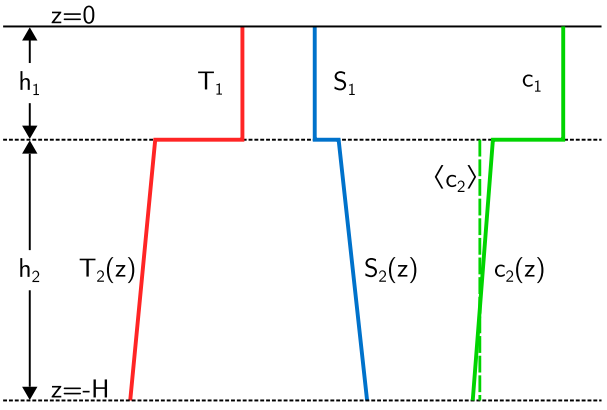

FIG. 6. Schematic of the two-layer model showing profiles of Conservative Temperature (T), Absolute Salinity (S), and sound speed (c) with depth.

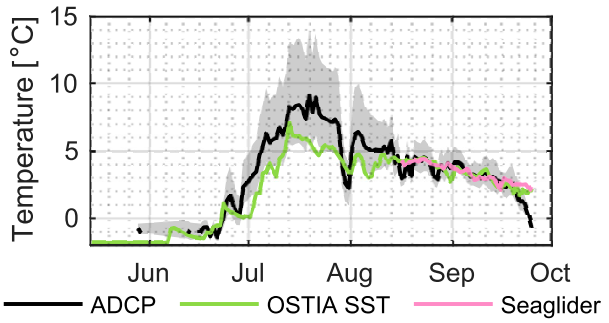

FIG. 7. ML temperatures (T_1) as determined using the ADCP with the sound speed model (black line) and from satellite SST (from OSTIA; green line) and the Seaglider measurements (pink line). The gray shaded area indicates the estimated uncertainty of T_1, obtained by simultaneously varying h_1 by ±3 m and d by ±0.05 m.

For a two-layer system, the vertical two-way travel time of an acoustic signal is

$$t_{2w} = 2\left(\frac{h_1}{\langle c_1\rangle} + \frac{h_2}{\langle c_2\rangle}\right), \tag{3}$$

where $\langle c_n\rangle$ is the harmonic mean of the depth varying sound speed in layer n: $\langle c_n\rangle = h_n[\int_{h_n} dz/c(z)]^{-1}$. As the ML is assumed to be homogeneous, $\langle c_1\rangle$ is approximately constant; sound speed does vary slightly with pressure, but the effects are negligible in this depth range. Equating Eq. (3) with the acoustic travel time inferred from the mooring altimeter distance [$t_{2w} = 2Dc(H)^{-1}$, where $c(H)$ is the speed of sound measured at the instrument at depth $H = h_1 + h_2$] gives an expression for the ML sound speed:

$$c_1 = c(H)\left[\left(1 - \frac{\varepsilon_D}{h_1}\right) + \left(1 - \frac{c(H)}{\langle c_2\rangle}\right)\left(\frac{h_2}{h_1}\right)\right]^{-1}, \tag{4}$$

where ε_D is the portion of the distance offset measurements that can be attributed to sound speed variation within the water column.

Inversion of c_1 to find the ML temperature requires some prescription of the ML salinity S_1. As the input of freshwater to the ML is a result of sea ice melt, an approximation for ML salinity is based on a conservation of salt mass within the sea ice and the water column:

$$h_1 S_1 + \int_{-H}^{-h_1} S_2(z)dz = d_e S_i + \int_{-H}^{-d_e} S_2(z)dz, \tag{5}$$

where d_e is an effective ice draft $d_e = (1 - A)d_i$ for A the fractional sea ice concentration (from satellite measurements) and d_i the average sea ice draft prior to the onset of melt (taken as 1.2 m), and S_i the sea ice salinity (taken as 6 g kg^{-1}). In this formulation, an assumed hydrostatic balance for sea ice was used to replace ice thickness with draft and eliminate density terms. This is equivalent to the "salt deficit" model used by Wilson et al. (2019) and to the sea ice melt-layer thickness model used by Peralta-Ferriz and Woodgate (2015, see their appendix A). Using the density profile associated with the modeled salinity, we also calculate ε_H. Values of ε_H were ~0.02 m during partial sea ice cover, and increased to ~0.04 m in open water; there was very little variation in calculated ε_H. Distance offset measurements ($H - D$) made in nonzero ice concentration (in gaps between ice floes; see Cooper et al. 2022) when the ML was deeper than the instrument (so $\varepsilon_D = 0$; blue points in Fig. 5, ~3% of measurements) cannot be fully explained by the calculated values of ε_H, so an additional empirical offset of 0.05 m was added to ε_H. Using these, $\varepsilon_D = d - \varepsilon_H$ from the distance offsets, d (from Fig. 5).

Equation (4) was applied to calculate c_1 with daily averaged values of ε_D, using h_1 from section 3 (and $h_2 = H - h_1$) and sound speeds $c(H)$ and $\langle c_2\rangle$ calculated from the modeled lower-layer profiles $T_2(z)$, $S_2(z)$ using functions provided in the Gibbs Seawater Oceanographic toolbox (IOC et al. 2010). Then, c_1 values were numerically inverted using the estimated ML salinity, S_1, to find the ML temperature, T_1. As sound speed is only weakly dependent on salinity, estimates of T_1 were insensitive to the modeled ML salinity (differences of ≤0.1°C compared to simply extending the S_2 profile to the surface). To assess the effect of uncertainties of the ML depth, and of the distance offset measurements, T_1 were recalculated while varying h_1 by ±3 m (corresponding with the summertime RMSE of h_1, cf. section 3), and d by ±0.05 m (roughly corresponding with the uncertainty of the ADCP pressure sensor).

b. Results

The sound speed model produces realistic ML temperatures (Fig. 7). Modeled temperatures exceeded satellite SSTs by up to ~3°C when temperatures peaked in mid-July, though satellite SSTs roughly overlapped with the lower uncertainty bound on temperature. From mid-August onward, the modeled ML temperature matched with both satellite SST and the ML temperature observed by Seagliders (Fig. 7). Correlation coefficients and root-mean-square errors between the ADCP-derived ML temperatures and the satellite SST product were $r = 0.89$ and RMSE = 1.46°C. For the Seaglider, they were $r = 0.79$ and RMSE = 0.85°C.

Uncertainties in T_1 resulting from simultaneously varying h_1 and d translated to a relatively large uncertainty range of +5°C to −3°C in ML temperature when h_1 was shallow (~15 m, in mid-July; Fig. 3), but had minimal impact on T_1 estimates for deeper MLs (±1°C in mid-August–October when h_1 ~ 25–30 m). When taken separately, the uncertainties in T_1 associated with varying either h_1 or d individually both have similar patterns, with peaks in mid-July (not shown). At the peak, h_1 variations of ±3 m result in an uncertainty in T_1 of +3°C to −2°C while d variations of ±0.05 m result in ±1.5°C differences in T_1 (the uncertainty varying them simultaneously is a nonlinear combination of the two). Later in the record (mid-August–October), the range of d gives an uncertainty in T_1 of ±0.7°C, and h_1 gives an uncertainty of ±0.3°C. The larger uncertainties in T_1 early in the record are the result of both the uncertainty being inversely proportional to h_1, and the fact that when h_1 is shallow, variations of ±3 m reflect a larger relative difference. The largest overestimates of T_1 relative to the satellite SST occur when the ML depth is not constrained by Seaglider measurements, and might suggest an underestimate of the ML depth. That the lower uncertainty bound of T_1 overlaps with the satellite SST during this period (Fig. 7) indicates that an increase of the estimated ML depth by ~3 m (from ~15 to ~18 m) would be sufficient to approximately recreate the observed SST.

Aside from uncertainty in the ML depth, the mismatch between satellite SST and ADCP-derived estimates of the ML temperature in July might be partly attributed to the simplicity of the two-layer model being applied here (Fig. 6), and partly to larger-scale (smoother) satellite SST estimates underestimating values relative to point measurements. Heat within some transition layer underneath the homogeneous ML (e.g., Price et al. 1986) would be misattributed here to higher ML temperatures. In applying a sound speed model to find the temperatures in Sermilik Fjord, Sanchez et al. (2021) fits hyperbolic-tangent profiles for temperature and salinity with some constant known interfacial thickness. A similar model might improve these results, though it is unlikely that the interfacial thickness would remain constant through the summer. There are also a variety of other reasons why in situ ML temperature measurements with satellite SST might disagree. There are challenges in determining SST from satellite measurements in the Beaufort Sea, and variability between different data products (Castro et al. 2016). Additionally, skin effects lead to temperature offsets between SST and the underlying ocean temperature (Minnett et al. 2019). Crews et al. (2022) found differences between in situ observations of surface temperature and satellite SST of ~1°C in the same study region (though of the opposite sign than suggested here, and using a different SST product). While further work is needed to address potential mismatches, the strong correlation between the satellite SST and ADCP-derived ML temperatures ($r = 0.89$) indicates the viability for prediction of ML temperatures from ADCP altimeter measurements.

5. Discussion

This study demonstrates that viable estimates of the surface ML depth and ML temperature can be made from upward-looking ADCPs installed on subsurface moorings. ML depths were estimated from a combination of maxima in both acoustic backscatter and inertial shear. Results were consistent with previous studies in the area, with winter depths of ~40 m and summer of ~15–20 m, and followed mooring and Seaglider measurements of the thermocline depth. Summertime ML temperatures at the southernmost mooring were estimated using an inverse sound speed model and produced results similar to satellite SST measurements, and matching those measured by an autonomous Seaglider.

Additional measurements could be used to improve and further validate the results from this study. This could include optimization of the algorithmic approaches for identifying the ML depth on shorter time scales, especially during the initial onset of the ice melt and the establishment of the summer shallow ML. It would be beneficial to further investigate approaches for identifying the timing of the shift to summer ML conditions; here that was done manually based on observed backscatter and shear properties, but it is possible that the timing could be linked to changes in sea ice conditions that would be detectable from remote sensing products. Improvements to ML temperature estimates could be made by using more realistic models of temperature/salinity stratification in the sound speed model.

As moorings in the sea ice covered Arctic Ocean lack surface expressions, these methods can be used to fill in observational gaps above the topmost float of subsurface moorings, and infer measurements of the surface ML that could be critical for better understanding ice–ocean interactions in this region. There are a number of long-term mooring records in the Arctic that include upward-looking ADCPs (e.g., Armitage et al. 2017; Lin et al. 2019; Polyakov et al. 2020a) for which the ML depth detection methods could be applied. While ADCPs with altimeters are less commonly deployed, the methods for temperature inversion from altimeter data could be similarly applied to stand-alone upward-looking sonars installed on some moorings (such as those in Krishfield et al. 2014).

Future mooring deployments can be designed to take advantage of these methods. For example, the newer *echo sounder* mode available on some Nortek Signature ADCPs (e.g., Velasco et al. 2018) can provide acoustic backscatter measurements at much higher fidelity and sensitivity and may facilitate easier identification of ML depth. These measurements can be available down to centimeter scales, greatly improving the accuracy and resolution of potential ML depth estimates. With some additional study, it may even be possible to link acoustic reflection measurements from these instruments to stratification strength (Shibley et al. 2020).

The ML properties derived here provide additional understanding and context for other observations from these moorings. For example, ML inertial oscillations, which have been shown to be highly seasonal in the Arctic (e.g., Plueddemann et al. 1998; Rainville and Woodgate 2009; Polyakov et al. 2020b) are also sensitive to the ML depth (D'Asaro 1985). Using this time series of ML depths together with mooring measurements of ML and sea ice velocities allows us to parse out different drivers of that seasonality.

Acknowledgments. This work was supported by the Office of Naval Research as part of the Stratified Ocean Dynamics of the Arctic (SODA) research project. Funding was provided by Grants N00014-18-1-2687 (Brenner), N00014-16-1-2349 (Thomson), N00014-14-1-2377 (Rainville and Lee), N00014-16-1-2348 (Doble), and N00014-16-1-2528 (Wilkinson). The authors thank Captain Greg Tlapa and Captain MaryEllen Durley, along with the rest of the command team and crew of USCGC *Healy* for operational support in 2018 and 2019. We would additionally like to thank Joe Talbert, Jason Gobat, Eric Boget, and Ben Jokinen (University of Washington, Applied Physics Laboratory) for mooring deployment/recovery and engineering support, and Lovro Valcic (Bruncin) for instrumentation engineering/design for the breakaway temperature chains.

Data availability statement. Data files containing the time series of the measurements and results described in this study are available at http://hdl.handle.net/1773/49495. More information about the project can be found at www.apl.washington.edu/soda.

REFERENCES

Ardyna, M., M. Babin, M. Gosselin, E. Devred, L. Rainville, and J.-É. Tremblay, 2014: Recent Arctic Ocean sea ice loss triggers novel fall phytoplankton blooms. *Geophys. Res. Lett.*, **41**, 6207–6212, https://doi.org/10.1002/2014GL061047.

Armitage, T. W. K., S. Bacon, A. L. Ridout, A. A. Petty, S. Wolbach, and M. Tsamados, 2017: Arctic Ocean surface geostrophic circulation 2003–2014. *Cryosphere*, **11**, 1767–1780, https://doi.org/10.5194/tc-11-1767-2017.

Brenner, S., L. Rainville, J. Thomson, S. Cole, and C. Lee, 2021: Comparing observations and parameterizations of ice-ocean drag through an annual cycle across the Beaufort Sea. *J. Geophys. Res. Oceans*, **126**, e2020JC016977, https://doi.org/10.1029/2020JC016977.

Castro, S. L., G. A. Wick, and M. Steele, 2016: Validation of satellite sea surface temperature analyses in the Beaufort Sea using UpTempO buoys. *Remote Sens. Environ.*, **187**, 458–475, https://doi.org/10.1016/j.rse.2016.10.035.

Chaudhuri, D., D. Sengupta, E. D'Asaro, and S. Shivaprasad, 2021: Trapping of wind momentum in a salinity-stratified ocean. *J. Geophys. Res. Oceans*, **126**, e2021JC017770, https://doi.org/10.1029/2021JC017770.

Cole, S. T., and Coauthors, 2017: Ice and ocean velocity in the Arctic marginal ice zone: Ice roughness and momentum transfer. *Elementa*, **5**, 55, https://doi.org/10.1525/elementa.241.

Cooper, V. T., L. A. Roach, J. Thomson, S. D. Brenner, M. M. Smith, M. H. Meylan, and C. M. Bitz, 2022: Wind waves in sea ice of the western Arctic and a global coupled wave-ice model. *Philos. Trans. Roy. Soc.*, **A380**, 20210258, https://doi.org/10.1098/rsta.2021.0258.

Crews, L., C. M. Lee, L. Rainville, and J. Thomson, 2022: Direct observations of the role of lateral advection of sea ice meltwater in the onset of autumn freeze up. *J. Geophys. Res. Oceans*, **127**, e2021JC017775, https://doi.org/10.1029/2021JC017775.

D'Asaro, E. A., 1985: The energy flux from the wind to near-inertial motions in the surface mixed layer. *J. Phys. Oceanogr.*, **15**, 1043–1059, https://doi.org/10.1175/1520-0485(1985)015<1043:TEFFTW>2.0.CO;2.

Deines, K., 1999: Backscatter estimation using broadband acoustic Doppler current profilers. *Proc. IEEE Sixth Working Conf. on Current Measurement*, San Diego, CA, IEEE, 249–253, https://doi.org/10.1109/CCM.1999.755249.

Dmitrenko, I. A., and Coauthors, 2020: Sea-ice and water dynamics and moonlight impact the acoustic backscatter diurnal signal over the eastern Beaufort Sea continental slope. *Ocean Sci.*, **16**, 1261–1283, https://doi.org/10.5194/os-16-1261-2020.

——, and Coauthors, 2021: Coastal polynya disrupts the acoustic backscatter diurnal signal over the eastern Laptev Sea shelf. *Front. Mar. Sci.*, **8**, 791096, https://doi.org/10.3389/fmars.2021.791096.

Donlon, C. J., M. Martin, J. Stark, J. Roberts-Jones, E. Fiedler, and W. Wimmer, 2012: The Operational Sea Surface Temperature and Sea Ice Analysis (OSTIA) system. *Remote Sens. Environ.*, **116**, 140–158, https://doi.org/10.1016/j.rse.2010.10.017.

Fine, E. C., and S. T. Cole, 2022: Decadal observations of internal wave energy, shear, and mixing in the western Arctic Ocean. *J. Geophys. Res. Oceans*, **127**, e2021JC018056, https://doi.org/10.1029/2021JC018056.

Francois, R. E., and G. R. Garrison, 1982: Sound absorption based on ocean measurements. Part II: Boric acid contribution and equation for total absorption. *J. Acoust. Soc. Amer.*, **72**, 1879–1890, https://doi.org/10.1121/1.388673.

Gallaher, S. G., T. P. Stanton, W. J. Shaw, S. T. Cole, J. M. Toole, J. P. Wilkinson, T. Maksym, and B. Hwang, 2016: Evolution of a Canada Basin ice-ocean boundary layer and mixed layer across a developing thermodynamically forced marginal ice zone. *J. Geophys. Res. Oceans*, **121**, 6223–6250, https://doi.org/10.1002/2016JC011778.

Gostiaux, L., and H. van Haren, 2010: Extracting meaningful information from uncalibrated backscattered echo intensity data. *J. Atmos. Oceanic Technol.*, **27**, 943–949, https://doi.org/10.1175/2009JTECHO704.1.

Harding, S., L. Kilcher, and J. Thomson, 2017: Turbulence measurements from compliant moorings. Part I: Motion characterization. *J. Atmos. Oceanic Technol.*, **34**, 1235–1247, https://doi.org/10.1175/JTECH-D-16-0189.1.

Holbrook, W. S., and I. Fer, 2005: Ocean internal wave spectra inferred from seismic reflection transects. *Geophys. Res. Lett.*, **32**, L15604, https://doi.org/10.1029/2005GL023733.

IOC, SCOR, and IAPSO, 2010: The International Thermodynamic Equation of Seawater—2010: Calculation and use of thermodynamic properties. Intergovernmental Oceanographic Commission, Manuals and Guides 56, 220 pp., https://www.teos-10.org/pubs/TEOS-10_Manual.pdf.

Kirillov, S., and Coauthors, 2020: Atmospheric forcing drives the winter sea ice thickness asymmetry of Hudson Bay. *J. Geophys. Res. Oceans*, **125**, e2019JC015756, https://doi.org/10.1029/2019JC015756.

Krishfield, R., J. Toole, A. Proshutinsky, and M.-L. Timmermans, 2008: Automated ice-tethered profilers for seawater observations under pack ice in all seasons. *J. Atmos. Oceanic Technol.*, **25**, 2091–2105, https://doi.org/10.1175/2008JTECHO587.1.

——, A. Proshutinsky, K. Tateyama, W. J. Williams, E. C. Carmack, F. A. McLaughlin, and M.-L. Timmermans, 2014: Deterioration of perennial sea ice in the Beaufort Gyre from 2003 to 2012 and its impact on the oceanic freshwater cycle. *J. Geophys. Res. Oceans*, **119**, 1271–1305, https://doi.org/10.1002/2013JC008999.

Lee, C. M., and Coauthors, 2016: Stratified ocean dynamics of the Arctic: Science and experiment plan. University of Washington Applied Physics Laboratory Tech. Rep. APL-UW-1601,

46 pp., https://apl.uw.edu/research/downloads/publications/tr_1601.pdf.

Lin, P., R. S. Pickart, G. W. K. Moore, M. A. Spall, and J. Hu, 2019: Characteristics and dynamics of wind-driven upwelling in the Alaskan Beaufort Sea based on six years of mooring data. *Deep-Sea Res. II*, **62**, 79–92, https://doi.org/10.1016/j.dsr2.2018.01.002.

Macrander, A., R. H. Käse, U. Send, H. Valdimarsson, and S. Jónsson, 2007: Spatial and temporal structure of the Denmark Strait Overflow revealed by acoustic observations. *Ocean Dyn.*, **57**, 75–89, https://doi.org/10.1007/s10236-007-0101-x.

Magnell, B., L. Ivanov, and E. Siegel, 2010: Measurements of ice parameters in the Beaufort Sea using the Nortek AWAC acoustic Doppler current profiler. *OCEANS 2010 MTS/IEEE Seattle*, Seattle, WA, IEEE, https://doi.org/10.1109/OCEANS.2010.5664016.

Meinen, C. S., and D. R. Watts, 1998: Calibrating inverted echo sounders equipped with pressure sensors. *J. Atmos. Oceanic Technol.*, **15**, 1339–1345, https://doi.org/10.1175/1520-0426(1998)015<1339:CIESEW>2.0.CO;2.

Minnett, P. J., and Coauthors., 2019: Half a century of satellite remote sensing of sea-surface temperature. *Remote Sens. Environ.*, **233**, 111366, https://doi.org/10.1016/j.rse.2019.111366.

Möller, K. O., M. S. John, A. Temming, J. Floeter, A. F. Sell, J.-P. Herrmann, and C. Möllmann, 2012: Marine snow, zooplankton and thin layers: Indications of a trophic link from small-scale sampling with the video plankton recorder. *Mar. Ecol. Prog. Ser.*, **468**, 57–69, https://doi.org/10.3354/meps09984.

Penrose, J., and T. Beer, 1981: Acoustic reflection from estuarine pycnoclines. *Estuarine Coastal Shelf Sci.*, **12**, 237–249, https://doi.org/10.1016/S0302-3524(81)80122-3.

Peralta-Ferriz, C., and R. A. Woodgate, 2015: Seasonal and interannual variability of pan-Arctic surface mixed layer properties from 1979 to 2012 from hydrographic data, and the dominance of stratification for multiyear mixed layer depth shoaling. *Prog. Oceanogr.*, **134**, 19–53, https://doi.org/10.1016/j.pocean.2014.12.005.

Plueddemann, A. J., R. Krishfield, T. Takizawa, K. Hatakeyama, and S. Honjo, 1998: Upper ocean velocities in the Beaufort Gyre. *Geophys. Res. Lett.*, **25**, 183–186, https://doi.org/10.1029/97GL53638.

Pollard, R. T., and R. C. Millard Jr., 1970: Comparison between observed and simulated wind-generated inertial oscillations. *Deep-Sea Res. Oceanogr. Abstr.*, **17**, 813–816, https://doi.org/10.1016/0011-7471(70)90043-4.

Polyakov, I. V., and Coauthors, 2020a: Intensification of near-surface currents and shear in the eastern Arctic Ocean. *Geophys. Res. Lett.*, **47**, e2020GL089469, https://doi.org/10.1029/2020GL089469.

——, and Coauthors, 2020b: Weakening of cold halocline layer exposes sea ice to oceanic heat in the eastern Arctic Ocean. *J. Climate*, **33**, 8107–8123, https://doi.org/10.1175/JCLI-D-19-0976.1.

Price, J. F., R. A. Weller, and R. Pinkel, 1986: Diurnal cycling: Observations and models of the upper ocean response to diurnal heating, cooling, and wind mixing. *J. Geophys. Res.*, **91**, 8411–8427, https://doi.org/10.1029/JC091iC07p08411.

——, ——, and R. R. Schudlich, 1987: Wind-driven ocean currents and Ekman transport. *Science*, **238**, 1534–1538, https://doi.org/10.1126/science.238.4833.1534.

Rainville, L., and R. A. Woodgate, 2009: Observations of internal wave generation in the seasonally ice-free Arctic. *Geophys. Res. Lett.*, **36**, L23604, https://doi.org/10.1029/2009GL041291.

Randelhoff, A., A. Sundfjord, and A. H. H. Renner, 2014: Effects of a shallow pycnocline and surface meltwater on sea ice–ocean drag and turbulent heat flux. *J. Phys. Oceanogr.*, **44**, 2176–2190, https://doi.org/10.1175/JPO-D-13-0231.1.

Ross, T., and A. C. Lavery, 2012: Acoustic scattering from density and sound speed gradients: Modeling of oceanic pycnoclines. *J. Acoust. Soc. Amer.*, **131**, EL54, https://doi.org/10.1121/1.3669394.

Sanchez, R., F. Straneo, and M. Andres, 2021: Using acoustic travel time to monitor the heat variability of glacial fjords. *J. Atmos. Oceanic Technol.*, **38**, 1535–1550, https://doi.org/10.1175/JTECH-D-20-0176.1.

Shcherbina, A., E. A. D'Asaro, B. Light, J. W. Deming, and E. Rehm, 2016: Maiden voyage of the under-ice float. *2016 Ocean Sciences Meeting*, New Orleans, LA, Amer. Geophys. Union, Abstract HE24A-1425, https://agu.confex.com/agu/os16/meetingapp.cgi/Paper/93130.

Shibley, N. C., M.-L. Timmermans, and C. Stranne, 2020: Analysis of acoustic observations of double-diffusive finestructure in the Arctic Ocean. *Geophys. Res. Lett.*, **47**, e2020GL089845, https://doi.org/10.1029/2020GL089845.

Stranne, C., and Coauthors, 2017: Acoustic mapping of thermohaline staircases in the Arctic Ocean. *Sci. Rep.*, **7**, 15192, https://doi.org/10.1038/s41598-017-15486-3.

——, and Coauthors, 2018: Acoustic mapping of mixed layer depth. *Ocean Sci.*, **14**, 503–514, https://doi.org/10.5194/os-14-503-2018.

Thomson, J., 2022: Wave propagation in the marginal ice zone: Connections and feedback mechanisms within the air–ice–ocean system. *Philos. Trans. Roy. Soc.*, **A380**, 20210251, https://doi.org/10.1098/rsta.2021.0251.

——, and W. E. Rogers, 2014: Swell and sea in the emerging Arctic Ocean. *Geophys. Res. Lett.*, **41**, 3136–3140, https://doi.org/10.1002/2014GL059983.

Toole, J. M., M.-L. Timmermans, D. K. Perovich, R. A. Krishfield, A. Proshutinsky, and J. A. Richter-Menge, 2010: Influences of the ocean surface mixed layer and thermohaline stratification on Arctic Sea ice in the central Canada Basin. *J. Geophys. Res.*, **115**, C10018, https://doi.org/10.1029/2009JC005660.

Tukey, J. W., 1961: Discussion, emphasizing the connection between analysis of variance and spectrum analysis. *Technometrics*, **3**, 191–219, https://doi.org/10.1080/00401706.1961.10489940.

Velasco, D. W., S. Nylund, and T. Pettersen, 2018: Combined current profiling and biological echosounding results from a single ADCP. *2018 OCEANS–MTS/IEEE Kobe Techno-Oceans*, Kobe, Japan, IEEE, https://doi.org/10.1109/OCEANSKOBE.2018.8559356.

Watts, D. R., and H. T. Rossby, 1977: Measuring dynamic heights with inverted echo sounders: Results from MODE. *J. Phys. Oceanogr.*, **7**, 345–358, https://doi.org/10.1175/1520-0485(1977)007<0345:MDHWIE>2.0.CO;2.

Wilson, E. A., S. C. Riser, E. C. Campbell, and A. P. S. Wong, 2019: Winter upper-ocean stability and ice–ocean feedbacks in the sea ice–covered Southern Ocean. *J. Phys. Oceanogr.*, **49**, 1099–1117, https://doi.org/10.1175/JPO-D-18-0184.1.